nature materials

Letter

https://doi.org/10.1038/s41563-022-01397-w

Planar thermal Hall effect of topological bosons in the Kitaev magnet α-$RuCl_3$

Received: 11 April 2022

Accepted: 4 October 2022

Published online: 17 November 2022

Check for updates

Peter Czajka[1], Tong Gao[1], Max Hirschberger[2], Paula Lampen-Kelley[3,4], Arnab Banerjee[5], Nicholas Quirk[1], David G. Mandrus[3,4], Stephen E. Nagler[6] & N. P. Ong[1]

The honeycomb magnet α-$RuCl_3$ has attracted considerable interest because it is proximate to the Kitaev Hamiltonian whose excitations are Majoranas and vortices. The thermal Hall conductivity κ_{xy} of Majorana fermions is predicted to be half-quantized. Half-quantization of κ_{xy}/T (T, temperature) was recently reported, but this observation has proven difficult to reproduce. Here, we report detailed measurements of κ_{xy} on α-$RuCl_3$ with the magnetic field B ∥ a (zigzag axis). In our experiment, κ_{xy}/T is observed to be strongly temperature dependent between 0.5 and 10 K. We show that its temperature profile matches the distinct form expected for topological bosonic modes in a Chern-insulator-like model. Our analysis yields magnon band energies in agreement with spectroscopic experiments. At high B, the spin excitations evolve into magnon-like modes with a Chern number of ~1. The bosonic character is incompatible with half-quantization of κ_{xy}/T.

The layered magnet, α-$RuCl_3$, is currently of intense interest because it is the closest known proximate to the Kitaev Hamiltonian $\mathcal{H}_K$ (refs. [1,2]). Each Ru ion, encaged within an octahedron of six Cl ions, has an effective spin-½ moment. Within a layer, the Ru ions define a honeycomb lattice spanned by lattice vectors **a** and **b**. In zero magnetic field, terms not included in $\mathcal{H}_K$ trigger a phase transition at 7 K to a zigzag antiferromagnetic state. The zigzag order is suppressed when the strength of a magnetic field **B** applied parallel to **a** exceeds 7.3 T. The striking absence of sharp magnetic excitation modes in the field interval $7.3 < B < 10$ T has led to considerable debate[3–11] on whether the in-plane field induces a quantum spin liquid[12]. Further interest has resulted from recent reports[13,14] that κ_{xy}/T is half-quantized in accord with the Majorana edge-mode prediction[1]. Here κ_{xy} is the planar thermal Hall conductivity and T the temperature. However, this half-quantization has been difficult to verify[15,16]. We report detailed measurements of κ_{xy} in α-$RuCl_3$ measured in the planar geometry with the magnetic field **B** ∥ **a**. We find that κ_{xy}/T is strongly T dependent with a profile matching that predicted for topological bosonic modes in the presence of a Berry curvature **Ω**. At large B, the spin excitations evolve into increasingly magnon-like modes with a Chern number of ~1. We contrast the distinctly bosonic character of κ_{xy} with half-quantization of κ_{xy}/T.

The thermal Hall effect provides a powerful probe of spin excitations, for example in the pyrochlores $Lu_2V_2O_7$ (ref. [17]) and $Tb_2Ti_2O_7$ (ref. [18]). The initial report[13] of half-quantization of κ_{xy}/T in α-$RuCl_3$ in a tilted **B** was followed by a report of half-quantization in the planar geometry (**B** ∥ **a**)[14]. However, a later experiment extended over a broad interval in T found no trace of half-quantized behaviour in κ_{xy}/T (ref. [15]). This was followed by yet another report finding robust quantization of the planar κ_{xy}/T (ref. [16]). These conflicting results reflect the weak signal and emergence of hysteretic and magnetocaloric effects below 4 K.

Adopting measures to mitigate these distortions (Methods and Supplementary Sections 1 and 2), we have obtained κ_{xy} over a broad interval of T (0.5 to 10 K). Our results point to a view of κ_{xy} categorically distinct from the half-quantized picture. We show that κ_{xy} originates from bosonic edge-mode excitations that become topological magnons at large B. Whereas fermionic edge modes have been investigated

[1]Department of Physics, Princeton University, Princeton, NJ, USA. [2]Department of Applied Physics, The University of Tokyo, Tokyo, Japan. [3]Department of Materials Science and Engineering, University of Tennessee, Knoxville, TN, USA. [4]Materials Science and Technology Division, Oak Ridge National Laboratory, Oak Ridge, TN, USA. [5]Department of Physics and Astronomy, Purdue University, West Lafayette, IN, USA. [6]Neutron Scattering Division, Oak Ridge National Laboratory, Oak Ridge, TN, USA. e-mail: npo@princeton.edu

https://doi.org/10.1038/s41563-022-01397-w

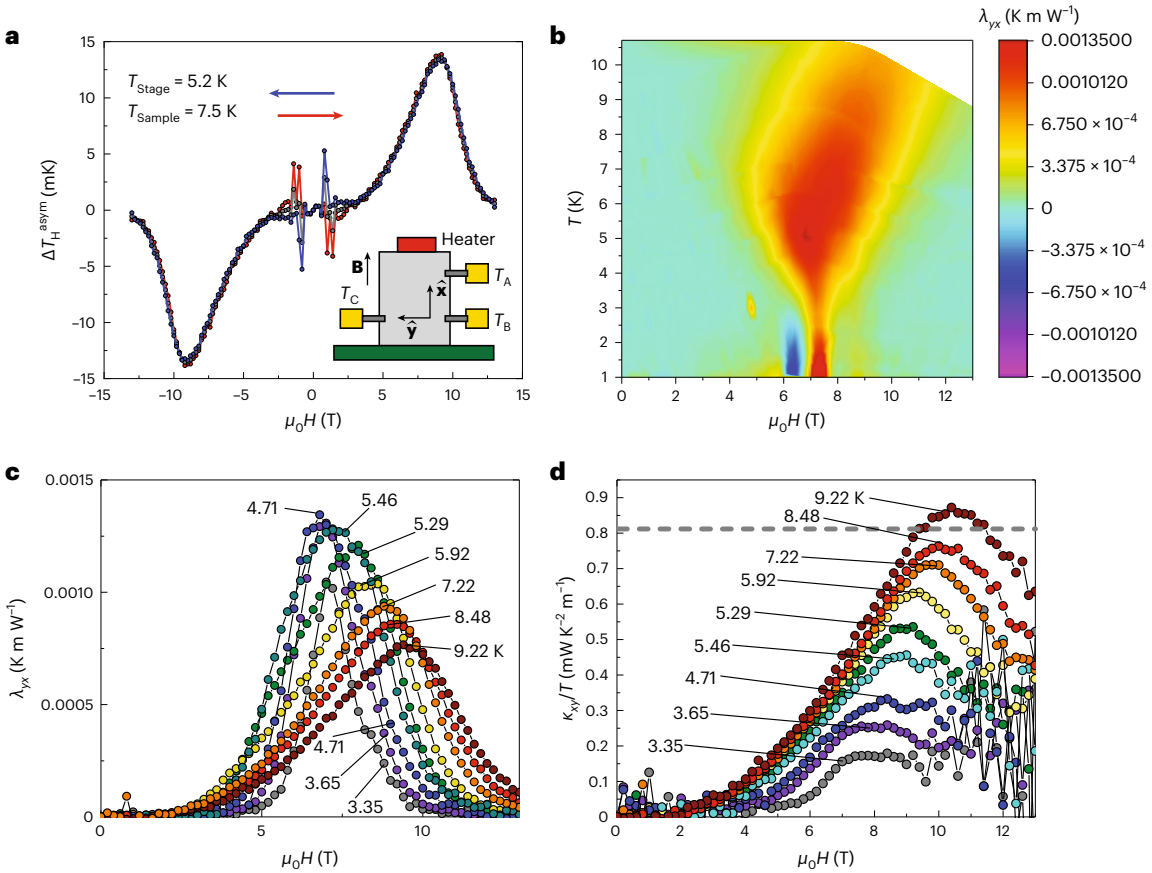

Fig. 1 | Planar thermal Hall response of α-$RuCl_3$ with B ∥ a. a, The *B*-antisymmetric thermal Hall signal ΔT_H^{asym} taken on sample S3 in sweep-up (red) and sweep-down (blue) directions at 7.5 K (ΔT_H^{asym} is proportional to λ_{yx}). The inset shows the placements of thermometers measuring T_A, T_B and T_C. T_{Stage}, the temperature of the stage; T_{Sample}, the temperature of the sample. **b**, The colour map constructed from ~50 traces of the thermal Hall resistivity λ_{yx} versus *B* in the *B*–*T* plane (scale bar on right). The large-λ_{yx} region (in red) tapers down to a neck around 7.3 T, as $T \to 0.4$ K. Below 2.5 K, $\lambda_{yx} < 0$ in a sliver at 6.3 T (blue region). **c**, Curves of λ_{yx} versus *B* at fixed *T*. The peak in the field profiles narrows as $T \to 3.35$ K. Below 4 K, λ_{yx} is strongly suppressed to zero above 9.5 T. **d**, Plots of κ_{xy}/T versus *B* (at fixed *T*) inferred from λ_{ij}. The non-intersecting curves imply that, at any fixed *B*, κ_{xy}/T is monotonic in *T*. Below 4.7 K the matrix inversion greatly amplifies the uncertainties in λ_{xy} for $B > 9$ T. The horizontal dashed line is the half-quantized value. The symbol μ_0 is the vacuum permeability.

intensively in quantum Hall effect systems, our experiment is a quantitative demonstration of κ_{xy} arising from neutral bosonic edge modes in a band with finite Chern number.

In the experiment, both the thermal current density $\mathbf{J}^Q$ and **B** are applied parallel to the (*x* axis) unit vector $\hat{\mathbf{x}}$ aligned with **a**. During each run lasting 8–10 h, *B* is changed in incremental steps of $\delta B_{step} = 0.2$ T from −13 to +13 T (and back to −13 T) while *T* is regulated within ±1 mK of its set point. We adopt a step–probe protocol (Methods) in which measurements of the sensors T_A, T_B and T_C are delayed by 150 s after each step change (Extended Data Figs. 1 and 2). The protocol rigorously excludes contamination by the large transients caused by magnetocaloric and eddy-current heating effects. Hysteretic artefacts are eliminated by combining field sweep-up and sweep-down curves. The three readings determine the values of the thermal Hall resistivity λ_{yx} and thermal resistivity λ_{xx} at each *B*. Data from samples S1 and S3 were obtained. In the main text we show data only from sample S3 (data for sample S1 are in Supplementary Section 6 and Supplementary Fig. 10).

Figure 1a shows the explicitly *B*-antisymmetric thermal Hall signal ΔT_H^{asym} (proportional to the thermal Hall resistivity λ_{yx}) measured at 7.5 K in an in-plane **B** ∥ $\hat{\mathbf{x}}$ (inset). At each *B*, the thermal Hall signal is obtained by combining the two readings $T_B - T_C$ and $T_A - T_C$, and field-antisymmetrizing (Supplementary Section 2). In Fig. 1b, the colour map provides an overview of how λ_{yx} varies over the *B*–*T* plane. The large-λ_{yx} region above 4 K (red area) tapers to a thin neck at 7.5 T as *T* decreases to 1 K. Below 2.5 K, λ_{yx} becomes slightly negative in the small region shown in blue. The evolution of the field profiles of λ_{yx} is shown in Fig. 1c. At 9.22 K, the profile features a broad peak that narrows dramatically as $T \to 3.65$ K. At high *B* (>10 T), λ_{yx} is strongly suppressed to values below our resolution for $T < 4$ K.

From the matrix inversion $\kappa_{ij} = [\lambda^{-1}]_{ij}$, we derive the curves of κ_{xy}/T versus *B*, which display a peak in the field profile (Fig. 1d). In the regime $B > 10$ T and $T < 4$ K, the matrix inversion leads to large uncertainties (caused by multiplying a near zero λ_{yx} by a factor of ~10^3 (Supplementary Section 2)). Over the interval 0.5 K < *T* < 10 K, κ_{xy}/T does not show evidence of half-quantization (corresponding to value given by the dashed line at 0.81; Supplementary Section 5). Instead, the dominant feature is the strong *T* dependence of κ_{xy}/T.

Figure 2 shows how κ_{xy}/T varies with *T* with *B* fixed at values between 5 and 10 T. At each value of *B*, κ_{xy}/T falls monotonically towards zero as *T* decreases below 10 K. We have found that the steep *T* dependence is in quantitative agreement with edge modes populated by bosons (solid curves).

Generally, a planar thermal Hall effect that is odd in **B** is quite unexpected. In topological materials, however, the emergence of a Berry curvature **Ω** that reverses sign with **B** can lead to a planar (electrical) Hall response, as seen in $ZrTe_5$ (ref. [19]). For this purpose, we would need **Ω** ∥ $\mathbf{c}^*$ ($\mathbf{c}^*$ is the unit vector normal to the honeycomb layer). In addition, **Ω** should reverse sign with **B** ∥ **a**.

https://doi.org/10.1038/s41563-022-01397-w

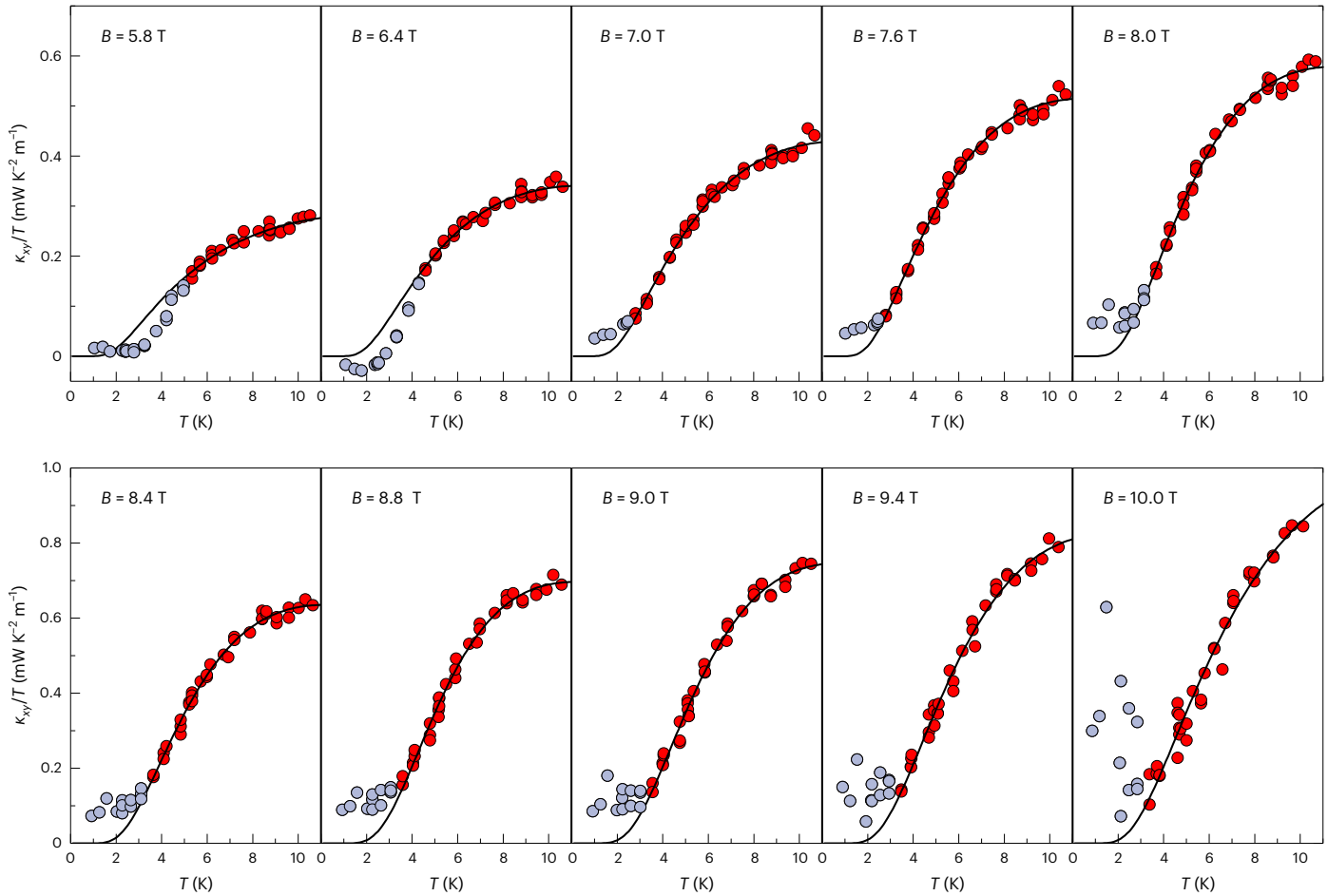

Fig. 2 | Curves of κ_{xy}/T versus T at selected values of B. In each panel, the solid curves are fits of data taken in sample S3 to Eqs (3) and (4). At each B, the fit yields the energies ω_1 and ω_2 and $\mathcal{C}_{\rm obs}$. The grey circles represent weak deviations from the fits below 4 K. Just below the boundary of the zigzag phase ($B < 7$ T), excitations in the zigzag state lead to negative deviations (also Fig. 3b). In the quantum spin liquid state (7 T < B < 11 T), positive deviations begin below 3 K and grow in amplitude as $T \to 0$. These seem to be related to the excitations that lead to oscillations in κ_{xx} (Supplementary Information).

Recent calculations have shown that $\mathbf{\Omega}$ indeed emerges in α-$RuCl_3$ with high-intensity spots near each of the corners of the Brillouin zone[8,9,20] (Fig. 3a, inset). At large B, the excitations, called topological magnons, occupy bands in which the Chern number $\mathcal{C}_n$ alternates in sign[8,9,20]. Crucially, when $\mathbf{B} \parallel \mathbf{a}$, $\mathbf{\Omega}$ reverses sign with $\mathbf{B}$[20–22].

In a two-dimensional magnet with finite $\mathbf{\Omega}$ (Supplementary Section 7), the thermal Hall conductivity is given by[23]

$$\frac{\kappa_{xy}}{T} = \frac{1}{\hbar V}\sum_{n,\mathbf{k}} \Omega_{n,z}(\mathbf{k}) \int_{\varepsilon_{n,\mathbf{k}}}^{\infty} \mathrm{d}\varepsilon \frac{(\varepsilon-\mu)^2}{T^2}\left(-\frac{\mathrm{d}\rho}{\mathrm{d}\varepsilon}\right), \qquad (1)$$

where the sum is over bands with dispersion $\varepsilon_{\mathbf{k}}$ and Berry curvature $\mathbf{\Omega}_n$, ρ is the distribution function of the relevant excitation, V is the sample volume, μ the chemical potential and $\hbar = h/2\pi$ with h the Planck constant.

Semiclassically, we may regard a wave packet subject to $\mathbf{\Omega}$ and the force $-\nabla U$ exerted by the wall potential U (ref. [23]; Fig. 3a, inset). The anomalous velocity $\mathbf{v}_{\rm A} = -\nabla U \times \mathbf{\Omega}$ drives a circulating thermal current around the edges. A thermal gradient $-\nabla T \parallel \hat{\mathbf{x}}$ unbalances the excitation density between the warm and cool edges ($\parallel \hat{\mathbf{y}}$, where $\hat{\mathbf{y}}$ is the unit vector along the y axis), which leads to a net thermal current $\mathbf{J}^{\rm Q} \parallel \hat{\mathbf{y}}$ (Fig. 3c). The reversal of $\mathbf{\Omega}$ induced by reversing $\mathbf{B}$ leads to an Onsager-type planar thermal Hall current.

If the excitations are fermions, Eq. (1) yields the (T-independent) Kane–Fisher result[24]

$$\frac{\kappa_{xy}}{T} = \frac{\pi^2}{3}\frac{k_{\rm B}^2}{h}\nu, \qquad (2)$$

where $k_{\rm B}$ is Boltzmann's constant and ν is an integer.

By contrast, for bosons, Eq. (1) yields a very strong T dependence. In units of the universal thermal conductance $k_{\rm B}^2/h$ (with μ set to 0), Eq. (1) simplifies to

$$\frac{\mathcal{K}_{\rm H}}{T} \equiv \frac{\kappa_{xy}/T}{k_{\rm B}^2/h} = \sum_n \mathcal{C}_n\, c_2^{(n)}(\omega_n, T), \qquad (3)$$

where $K_{\rm H}$ is the thermal Hall conductivity divided by the universal thermal conductance. The function $c_2^{(n)}(\omega_n, T)$ is defined as[23]

$$c_2^{(n)}(\omega_n, T) = \int_{u_{0n}}^{\infty} \mathrm{d}u\, u^2(-\mathrm{d}\rho/\mathrm{d}u), \quad (u_{0n} = \beta\omega_n(\mathbf{k})), \qquad (4)$$

where $\rho = 1/(\mathrm{e}^u - 1)$ and $\beta = 1/(k_{\rm B}T)$. In Eq. (4), $\omega_{\rm n}(\mathbf{k})$ is the energy at wavevector $\mathbf{k}$ in band n, and the integration variable u is the energy divided by $k_{\rm B}T$. The lowest band is nearly flat[20]. Adopting the flat-band approximation (Supplementary Section 7), we used the

https://doi.org/10.1038/s41563-022-01397-w

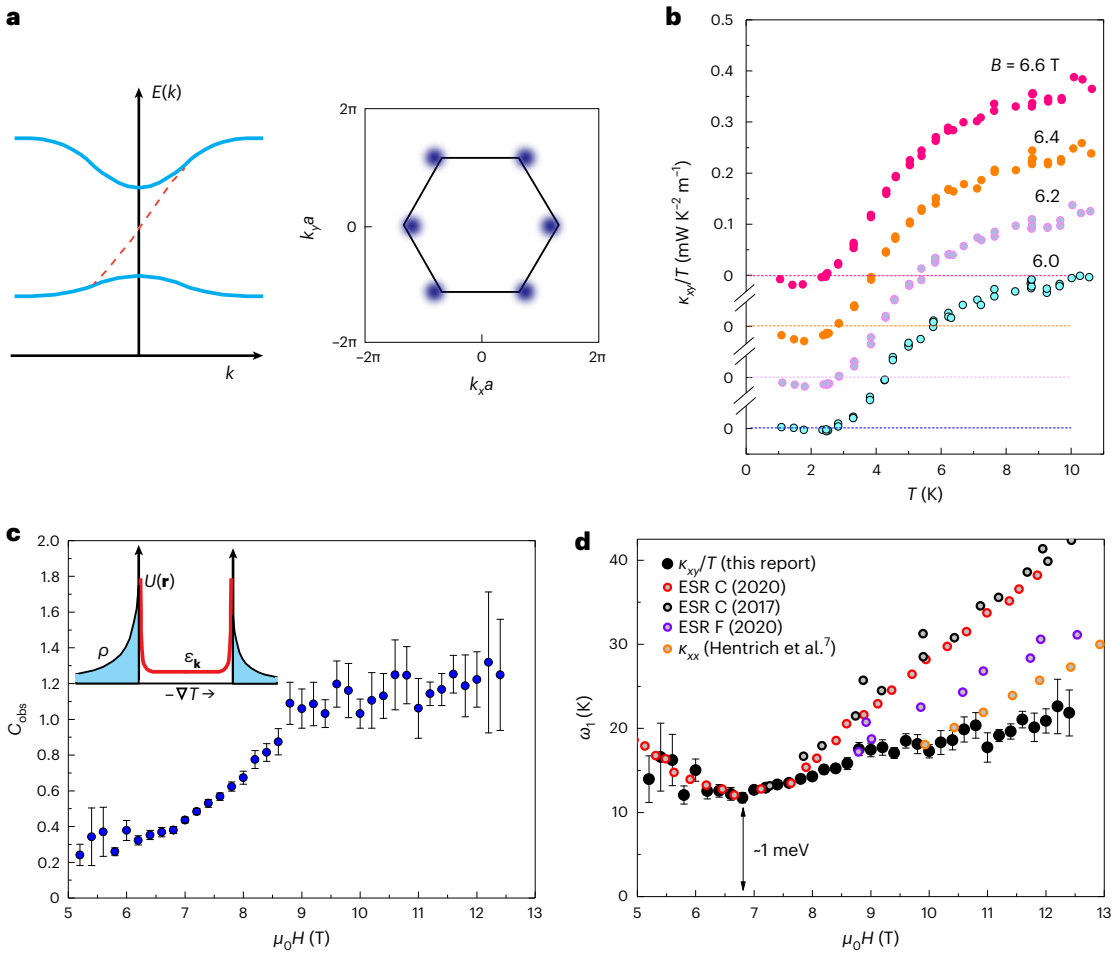

Fig. 3 | Bosonic edge mode and the planar κ_{xy}. **a**, Sketch of the energy $E(\mathbf{k})$ of the two lowest magnon modes (blue curves) with $\omega_1 = 11.6$ K and $\omega_2 \approx 50$ K. With $\mathcal{C} = 1$ in the lowest band, an edge mode traverses the gap (dashed curve). The inset displays the high-intensity spots of the Berry curvature $\mathbf{\Omega}$ in $\mathbf{k}$ space calculated[20] for the lowest band with $\mathbf{B} \parallel \mathbf{a}$. Points inside the Brillouin zone are given by (k_x, k_y) with a the lattice spacing. The Berry curvature $\mathbf{\Omega}$ changes sign with $\mathbf{B}$. **b**, Curves of κ_{xy}/T versus T in sample S3 with B fixed at 6.0, 6.2, 6.4 and 6.6 T (just inside the zigzag phase). Below 3 K, κ_{xy} displays a weak negative contribution. For clarity, we have shifted successive curves vertically by 0.1 mW K^{-2} m^{-1}. **c**, The quantity $\mathcal{C}_{obs}$ defined in Eq. (8) derived from the fit at each B. As B increases, $\mathcal{C}_{obs}$ saturates to a value ~1.1 above 9 T, consistent with the Chern integer 1. In the inset, the profile of $U(\mathbf{r}) + \omega_1$ is sketched as the red curve ($U(\mathbf{r})$ is the wall potential as a function of spatial coordinate $\mathbf{r}$ and ω_1 is the energy of the lowest band; here $\varepsilon_k = \omega_1$). A gradient $-\nabla T \parallel \hat{\mathbf{x}}$ unbalances the excitation densities between the warm and cool edges to produce $\mathbf{J}^Q \parallel \hat{\mathbf{y}}$ (distribution ρ shaded in blue). **d**, The B dependence of the energy level ω_1 derived from the fit of κ_{xy}/T versus T to Eq. (7) at each B. At the minimum (at 6.8 T), ω_1 agrees with the energy of the narrow mode (~1 meV) seen in electron spin resonance (ESR). At large B, ω_1 is slightly lower than the electron spin resonance modes (C and F), and in better agreement with the energy extracted from κ_{xx} in the literature[7]. In **c** and **d**, each symbol (at a particular value of H) is derived from the best fit of the curve κ_{xy}/T versus T to Eqs (3) and (4) performed using Mathematica's NonlinearModelFit program. The fit at each value of H involves $N = 30$–40 independent data points. The error bars are the standard error of the fit.

winding-number equation $2\pi\mathcal{C}_n = \int_{BZ} \mathrm{d}^2k\, \mathbf{\Omega}_{n,z}(\mathbf{k})$ to relate $\mathbf{\Omega}_{n,z}$ to $\mathcal{C}_n$ (BZ, Brillouin zone).

At low T, we retain the two lowest bands in Eq. (3) (Fig. 3a and Supplementary Section 7). Assuming that their Chern numbers alternate in sign ($\mathcal{C}_1 = -\mathcal{C}_2$), we have

$$\frac{\mathcal{K}_H}{T} = \mathcal{C}_1 \left[c_2^{(1)}(\omega_1, T) - c_2^{(2)}(\omega_2, T) \right]. \quad (5)$$

The overall scale of $\mathcal{K}_H/T$ is fixed by $\mathcal{C}_1$.

We find that Eq. (7) provides close fits to the observed κ_{xy}/T over a broad range of B (the fits were carried out on $\kappa_{xy}^{2D} = \kappa_{xy} d$ with $d = 5.72$ Å). In Fig. 2, the fits are shown as the solid curves. We have found that slight deviations from the fits (grey circles) reveal important information on the excitations.

For $B < 6.8$ T, κ_{xy}/T displays a weak, negative deviation (dip) below 3 K (in the blue region in Fig. 1b). The expanded view in Fig. 3b shows the dips in four traces of κ_{xy}/T versus T. The negative dips imply that, once we enter the ordered phase (below 7 T), the spin excitation branches deviate from Eq. (3). The weak negative dip feature also appears in calculations of κ_{xy} (Figs. 3 and 6 in a literature study[21]). Weak, positive deviations are also observed below ~11 T. These deviations may represent the growth of excitations in the quantum spin liquid state as $T \to 0$. Within the uncertainties, they scale with the amplitude of the oscillations in the thermal conductivity κ_{xx} (Supplementary Fig. 11).

Away from these deviations, the fits shown in Fig. 2 describe quite accurately the strong T dependence of κ_{xy}/T over a broad range of B. At each B, the fit yields the two band energies ω_1 and ω_2 (in Eq. (6)) as well as the dimensionless quantity $\mathcal{C}_{obs}$ discussed next.

Dividing Eq. (7) by the T-dependent factor $[c_2^{(1)}(\omega_1, T) - c_2^{(2)}(\omega_2, T)]$, we define

$$\mathcal{C}_{obs} \equiv (\mathcal{K}_H/T)/[c_2^{(1)}(\omega_1, T) - c_2^{(2)}(\omega_2, T)], \quad (6)$$

which can be compared with $\mathcal{C}_1$. $\mathcal{C}_{obs}$ is plotted versus B in Fig. 3c.

We find that $\mathcal{C}_{obs}$ starts off small (~0.3 at 5 T) but increases to attain a plateau profile above 9 T. Within the experimental uncertainty, the nearest integer at the plateau is $\mathcal{C}_{obs} \approx 1$. The strong T dependence of κ_{xy}/T largely arises from the bosonic distribution in the integrand of $c_2^{(n)}$ (Eq. (6)). Remarkably, once this is factored out, the overall amplitude in the polarized state at high fields is fixed by the integer $\mathcal{C}_{obs} \approx 1$. Supplementary Fig. 10 shows parameters from sample S1.

We show next that the energy ω_1 derived from the fits of κ_{xy}/T to Eq. (1) closely agrees with the energy of the dominant sharp mode seen in electron spin resonance[25,26], microwave absorption[27] and neutron-scattering experiments[28]. The energy of the second band is found to be $\omega_2 \approx 50 \pm 10$ K with a large uncertainty (Supplementary Section 6). In the field interval above the critical field B_c (from 7.3 to 14 T), α-$RuCl_3$ displays a rich magnetic resonance spectrum with four sharp modes (C, D, E and F)[25] superposed on a broad continuum suggestive of excitations[27]. The broad continuum was observed also in microwave absorption and inelastic neutron-scattering experiments[28]. At $B = 7.3$ T, the two lowest modes C and F are degenerate at 0.27 THz (1.1 meV). As B is increased to 16 T, both increase steeply, to 1.1 THz (for C) and 0.9 THz (for F). These modes are also seen in exact diagonalization of a 24-spin model[29]. Close to B_c, ω_1 inferred from κ_{xy}/T agrees remarkably well with the degenerate values of C and F. At large B, ω_1 is lower in energy than mode C (C arises from vertical transitions at the zone centre Γ with change in momentum $\Delta\mathbf{q} = 0$ (ref. [26]). This suggests that, as C rises steeply with B, κ_{xy} is weighted towards lower-lying excitations from elsewhere in the Brillouin zone. The curve of $\omega_1(B)$ is consistent with the energy scale inferred in the literature[7] from $\kappa_{xx}(T)$.

As discussed[25,26], the sharp electron spin resonance mode C is increasingly dominant at large B, but the broad background excitation continuum persists. From this viewpoint, the observed saturation of $\mathcal{C}_{obs}$ to 1 above 9 T in Fig. 3d is physically appealing. As the dominant excitations become increasingly magnon-like, the topological Hall current, expressed as $\mathcal{C}_{obs}$, approaches 1. For $B < 7$ T (zigzag state) the vanishing of κ_{xy} (aside from the negative dip near 6.3 T) suggests that $\mathbf{\Omega}$ is very small. Our results also conclusively rule out a phonon mechansim for the planar κ_{xy} (Supplementary Fig. 12 and Supplementary Section 9).

The physical picture that emerges is that the planar κ_{xy} derives from spin excitations that live at the relatively high energy scale $\omega_1 \approx 1$ meV (12 K) and form a bosonic Chern-insulator-like state at high B (with μ fixed at 0). A large Berry curvature drives these excitations as an edge-mode thermal current, which results in an Onsager-type thermal Hall current whose magnitude corresponds to a Chern number of 1 at fields above 9 T. At all B, the bosonic character leads to strong suppression of κ_{xy} to near zero below 3 K. The strong T dependence of κ_{xy}/T precludes a fermionic description and raises questions about the half-quantization as well as its robustness (Supplementary Section 6). We emphasize that the sharp magnon-like modes quite abruptly become unresolved at ~9 T (ref. [28]), which is consistent with the steep decrease of $\mathcal{C}_{obs}$ (Fig. 3c). From the electron spin resonance and microwave absorption experiments, the sharp modes coexist with a broad continuum of excitations. Hence ω_1 does not define a bulk 'spin gap' (the broad continuum extends well below it). Below 3 K, the edge-mode engendered κ_{xy} vanishes while a different set of bulk features emerges to define the oscillations observed in κ_{xx} (refs. [15,30]). At present, there is considerable debate on whether the intermediate state at $7\text{ T} < B < 12$ T is a spin liquid. The search for a sharp transition between the proposed spin liquid and the high-field polarized state is actively ongoing (calculations[29] do not see this transition; more information is in the literature[10]). Aside from uncovering the thermal Hall effect from topological magnons, the present κ_{xy} results may prove valuable in redirecting this search along more fruitful avenues.

Online content

Any methods, additional references, Nature Research reporting summaries, source data, extended data, supplementary information, acknowledgements, peer review information; details of author contributions and competing interests; and statements of data and code availability are available at https://doi.org/10.1038/s41563-022-01397-w.

References

1. Kitaev, A. Anyons in an exactly solved model and beyond. *Ann. Phys.* **321**, 2–111 (2006).
2. Jackeli, G. & Khaliullin, G. Mott insulators in the strong spin-orbit coupling limit: from Heisenberg to a quantum compass and Kitaev models. *Phys. Rev. Lett.* **102**, 017205 (2009).
3. Plumb, K. W. et al. α–$RuCl_3$: a spin-orbit assisted Mott insulator on a honeycomb lattice. *Phys. Rev. B* **90**, 041112 (2014).
4. Banerjee, A. et al. Proximate Kitaev quantum spin liquid behavior in a honeycomb magnet. *Nat. Mater.* **15**, 733–740 (2016).
5. Leahy, I. A. et al. Anomalous thermal conductivity and magnetic torque response in the honeycomb magnet α–$RuCl_3$. *Phys. Rev. Lett.* **118**, 187203 (2017).
6. Banerjee, A. et al. Excitations in the field-induced quantum spin liquid state of α-$RuCl_3$. *npj Quantum Mater.* **3**, 8 (2018).
7. Hentrich, R. et al. Unusual phonon heat transport in α–$RuCl_3$: strong spin-phonon scattering and field-induced spin gap. *Phys. Rev. Lett.* **120**, 117204 (2018).
8. McClarty, P. A. et al. Topological magnons in Kitaev magnets at high fields. *Phys. Rev. B* **98**, 060404 (2018).
9. Joshi, D. G. Topological excitations in the ferromagnetic Kitaev-Heisenberg model. *Phys. Rev. B* **98**, 060405 (2018).
10. Gordon, J. S., Catuneanu, A., Sørensen, E. S. & Kee, H.-Y. Theory of the field-revealed Kitaev spin liquid. *Nat. Commun.* **10**, 2470 (2019).
11. Hickey, C. & Trebst, S. Emergence of a field-driven U(1) spin liquid in the Kitaev honeycomb model. *Nat. Commun.* **10**, 530 (2019).
12. Savary, L. & Balents, L. Quantum spin liquids: a review. *Rep. Prog. Phys.* **80**, 106502 (2017).
13. Kasahara, Y. et al. Majorana quantization and half-integer thermal quantum Hall effect in a Kitaev spin liquid. *Nature* **559**, 227–231 (2018).
14. Yokoi, T. et al. Half-integer quantized anomalous thermal Hall effect in the Kitaev candidate α-$RuCl_3$. *Science* **373**, 568–572 (2021).
15. Czajka, P. et al. Oscillations of the thermal conductivity in the spin-liquid state of α-$RuCl_3$. *Nat. Phys.* **17**, 915–919 (2021).
16. Bruin, J. A. N. et al. Robustness of the thermal Hall effect close to half-quantization in α-$RuCl_3$. *Nat. Phys.* **18**, 401–405 (2022).
17. Onose, Y. et al. Observation of the magnon Hall effect. *Science* **329**, 297–299 (2011).
18. Hirschberger, M., Krizan, J. W., Cava, R. J. & Ong, N. P. Large thermal Hall conductivity of neutral spin excitations in a frustrated quantum magnet. *Science* **348**, 106–109 (2015).
19. Liang, T. et al. Anomalous Hall effect in $ZrTe_5$. *Nat. Phys.* **14**, 451–455 (2018).
20. Chern, L. E., Zhang, E. Z. & Kim, Y. B. Sign structure of thermal Hall conductivity and topological magnons for in-plane field polarized Kitaev magnets. *Phys. Rev. Lett.* **126**, 147201 (2021).
21. Zhang, E. Z., Chern, L. E. & Kim, Y. B. Topological magnons for thermal Hall transport in frustrated magnets with bond-dependent interactions. *Phys. Rev. B* **103**, 174402 (2021).
22. Utermohlen, F. G. & Trivedi, N. Symmetry analysis of tensors in the honeycomb lattice of edge-sharing octahedra. *Phys. Rev. B* **103**, 155124 (2021).
23. Matsumoto, R. & Murakami, S. Rotational motion of magnons and the thermal Hall effect. *Phys. Rev. B* **84**, 184406 (2011).
24. Kane, C. L. & Fisher, M. P. A. Quantized thermal transport in the fractional quantum Hall effect. *Phys. Rev. B* **55**, 15832 (1997).
25. Ponomaryov, A. N. et al. Unconventional spin dynamics in the honeycomb-lattice material α–$RuCl_3$: high-field electron spin resonance studies. *Phys. Rev. B* **96**, 241107(R) (2017).

26. Ponomaryov, A. N. et al. Nature of magnetic excitations in the high-field phase of α–$RuCl_3$. *Phys. Rev. Lett.* **125**, 037202 (2020).
27. Wellm, C. et al. Signatures of low-energy fractionalized excitations in α–$RuCl_3$ from field-dependent microwave absorption. *Phys. Rev. B* **98**, 184408 (2018).
28. Balz, C. et al. Finite field regime for a quantum spin liquid in α–$RuCl_3$. *Phys. Rev. B* **100**, 060405(R) (2019).
29. Winter, S. M., Riedl, K., Kaib, D., Coldea, R. & Valenti, R. Probing α–$RuCl_3$ beyond magnetic order: effects of temperature and magnetic field. *Phys. Rev. Lett.* **120**, 077203 (2018).
30. Villadiego, I. S. Pseudoscalar U(1) spin liquids in α–$RuCl_3$. *Phys. Rev. B* **104**, 195149 (2021).

Methods

The mounting procedure used for the sample follows the procedure described in detail in ref. [15]. A photo of the crystal and thermometer set-up used in this report is shown in Extended Data Fig. 1. The thermometers (RX102A) are connected to the crystal using Stycast epoxy via 5 mil Au wires (which themselves are attached to the thermometers using Ag epoxy). The ceramic heater (resistance, $R = 1\,\mathrm{k}\Omega$) is attached directly to the crystal using Ag paint. The crystal is also attached to a brass plate using Ag paint. To avoid damage caused by the large magnetic torque above 3 T, the other end of the crystal is mechanically supported using a piece of Delrin (a low thermal conductivity polymer) attached using Stycast epoxy. Once mounted, the brass plate is placed onto a Janis ^{3}He insert. Special care must be taken to not overstrain the crystal at any point, as even small amounts of mechanical stress may induce unwanted stacking faults in the crystal. To minimize electrical noise, all thermometers (sample and stage) are measured using Lakeshore LS372 temperature controllers. The LS372 uses a method based on a.c. lock-in that is optimized for temperature measurements and that offers much better resolution than d.c.-based Lakeshore models like the LS340 as well as conventional lock-in amplifiers.

The thermal transport tensor is calculated using a standard steady-state technique. A thermal current density $\mathbf{J}^{\mathrm{Q}}$ is applied using the 1 kΩ heater. We define $\hat{\mathbf{x}} \parallel \mathbf{J}^{\mathrm{Q}}$ and $\hat{\mathbf{z}} \parallel \mathbf{c}^*$ so $\hat{\mathbf{y}}$ is the transverse/Hall direction. The thermal resistivity matrix is analogous to the electrical equivalent and relates the applied current $\mathbf{J}^{\mathrm{Q}}$ to the resulting temperature gradient ∇T:

$$-\partial_i T = \lambda_{ij} J_j^{\mathrm{Q}}$$

In the experiment we measure the longitudinal and transverse temperature differences ($\Delta_x T$ and $\Delta_y T$, measured along the x and y axes, respectively). From these values, $\mathbf{J}^{\mathrm{Q}}$ and the appropriate sample dimensions, we are able to calculate all components of λ_{ij} and then invert the resulting matrix to obtain the thermal conductivity matrix $\kappa_{ij} = (\lambda^{-1})_{ij}$. We stress that it is only the field-antisymmetric component of Δ_y that is used in the above calculation, and it is this value (referred to as $\Delta T_{\mathrm{H}}{}^{\mathrm{asym}}$) that is the most essential quantity that is measured in these experiments. Crucial steps were taken to remove all extrinsic contributions to the measured $\Delta T_{\mathrm{H}}{}^{\mathrm{asym}}$. Our approach is to increase the magnetic field by steps of 0.2 T (steps spaced by 180 s). Once a new field value is reached, we wait for the thermometers to relax to their equilibrium temperatures. Extended Data Fig. 2 shows an example of this during data collection. The transient temperature shifts that ultimately relax are caused by eddy currents in the measurement apparatus and the unusually large magnetocaloric effects in α-$RuCl_3$. When analysing the data, we choose an averaging window (light blue strip shown in the inset) that contains only data acquired after equilibrium is attained.

More information about the technical details of our measurements can be found in Supplementary Sections 1 and 2.

Data availability

All data are archived in Dataverse: https://dataverse.harvard.edu/dataset.xhtml?persistentId=doi:10.7910/DVN/S6HAKK.

Acknowledgements

We acknowledge useful discussions with I. Sodemann and S. Todadri. P.C., T.G., N.Q. and N.P.O. were supported by the US Department of Energy (DE-SC0017863), by a Materials Research Science and Engineering Centers award from the US National Science Foundation (DMR 2011750) and by the Gordon and Betty Moore Foundation EPiQS initiative through grant GBMF9466 (to N.P.O.). A.B. and S.E.N. were supported by the Quantum Science Center, a National Quantum Information Science Research Center of the US Department of Energy. P.L.-K. and D.G.M. were supported by the Gordon and Betty Moore Foundation's EPiQS initiative through grant GBMF9069.

Author contributions

P.C. performed the measurements and analysed the data with N.P.O.; P.C., T.G. and N.P.O. conceptualized the experiment, which employs a methodology developed by them and M.H. The crystals were grown and characterized at Oak Ridge National Laboratory by P.L.-K., A.B., D.G.M. and S.E.N.; N.Q. performed the precision measurements of the experimentally relevant sample dimensions. The manuscript was written by P.C. and N.P.O. with input from all authors.

Competing interests

The authors declare no competing interests.

Additional information

Extended data is available for this paper at https://doi.org/10.1038/s41563-022-01397-w.

Supplementary information The online version contains supplementary material available at https://doi.org/10.1038/s41563-022-01397-w.

Correspondence and requests for materials should be addressed to N. P. Ong.

Peer review information *Nature Materials* thanks Joseph P. Heremans and the other, anonymous, reviewer(s) for their contribution to the peer review of this work.

https://doi.org/10.1038/s41563-022-01397-w

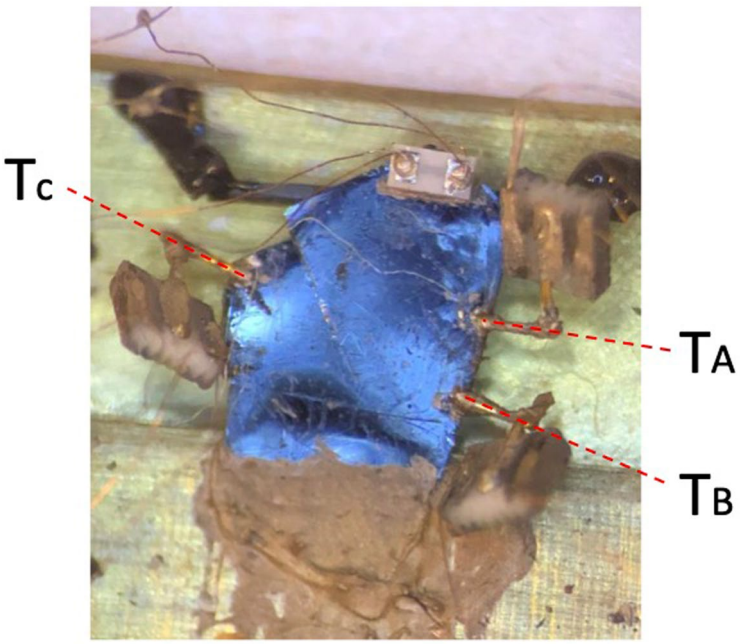

Extended Data Fig. 1 | Image of crystal S3. The three thermometers used for temperature measurements are labeled (T_A, T_B, T_C) as shown.

https://doi.org/10.1038/s41563-022-01397-w

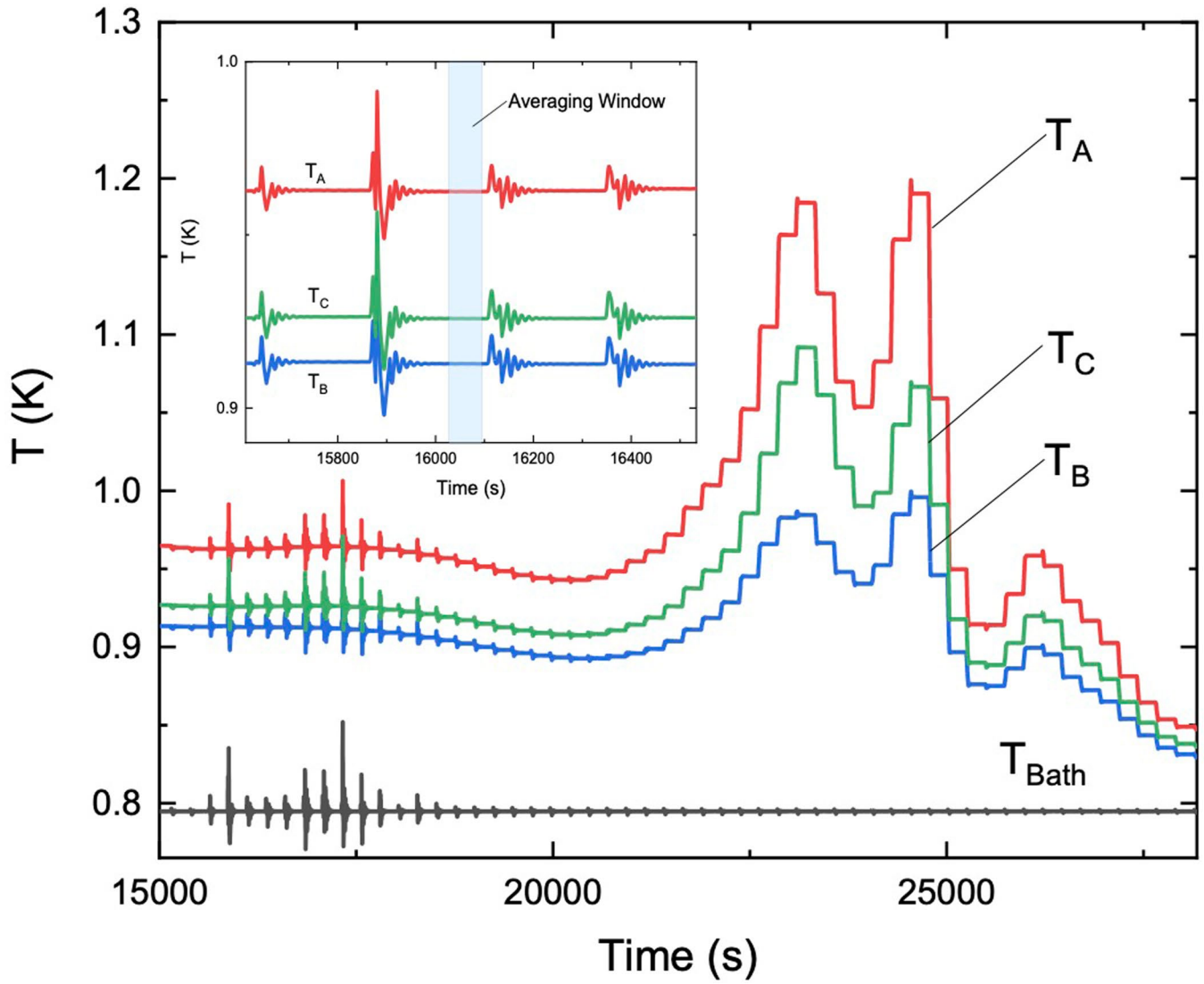

Extended Data Fig. 2 | Time trace of temperature readings in a field-step sequence. The inset depicts the same data over a narrower time window so that the timescales for the relaxation process can be seen.